Three-dimensional numerical modeling of an induction heated injection molding tool with flow visualization

Guerrier, Patrick; Tosello, Guido; Nielsen, Kaspar Kirstein; Hattel, Jesper Henri

Published in:
International Journal of Advanced Manufacturing Technology

Link to article, DOI:
10.1007/s00170-015-7955-8

Publication date:
2016

Document Version
Peer reviewed version

THREE-DIMENSIONAL NUMERICAL MODELING OF AN INDUCTION HEATED INJECTION MOLDING TOOL WITH FLOW VISUALIZATION

P. Guerrier[a,*], G. Tosello[a], Kaspar Kirstein Nielsen[b], J. H. Hattel[a]

[a]*Department of Mechanical Engineering, Technical University of Denmark, Produktionstorvet Building 425, 2800 Kgs. Lyngby*

[b] *Department of Energy Conversion and Storage, Technical University of Denmark, Frederiksborgvej 399, Building 779, 4000 Roskilde, Denmark*

[*]*Corresponding author, email address: pagu@mek.dtu.dk*

Abstract

Using elevated mold temperature is known to have a positive influence of final injection molded parts. Induction heating is a method that allow obtaining a rapid thermal cycle, so the overall molding cycle time is not increased. In the present research work, an integrated multiturn induction heating coil has been developed and assembled into an injection molding tool provided with a glass window, so the effect of induction heating can directly be captured by a high speed camera. In addition, thermocouples and pressure sensors are also installed, and together with the high speed videos, comparison of the induction heating and filling of the cavity is compared and validated with simulations. Two polymer materials ABS and HVPC were utilized during the injection molding experiments carried out in this work. A nonlinear electromagnetic model was employed to establish an effective linear magnetic permeability. The three-dimensional transient thermal field of the mold cavity was then calculated and compared with the experiments. This thermal field was transferred to an injection molding flow solver to compare simulations and experimental results from the high speed video, both with and without the effect of induction heating. A rapid thermal cycle was proved to be feasible in a mold with an integrated induction coil. Furthermore, it was shown that the process can be modeled with good accuracy, both in terms of the thermal field and of the flow pattern.

Keywords: Injection molding · Induction heating · Simulation · Rapid thermal process · Variotherm

1 Introduction

Rapid thermal cycling is a known method in the field of injection molding. The principle is to have a high mold temperature at the surface of the cavity during injection and packing, while having a low temperature during cooling. The hot surface during filling has many advantages, since it prevents the polymer from freezing and creating a skin layer, thus reducing the required pressure to fill the cavity. On the other hand, a cold surface is desired in the cooling phase to reduce the cooling time. In conventional injection molding, a cold mold is often chosen to reduce the overall cycle time, but this increases the requirement for the injection pressure and can cause problems in filling micro cavities, nano-structured surfaces or features that have a large length-to-thickness ratio. Other problems that are remedied when using a hot mold include weld lines, residual stresses, and part surface quality. This calls for a method to increase the mold

temperature above the phase transition temperature during filling and packing, while retaining a cold mold during the cooling phase.

There exists different approaches to get a rapid thermal cycle, including some of the more common such as resistive heating, infrared heating, induction heating, proximity heating, hot fluid, and passive heating [1]. The general concept is that the mold needs a low thermal mass and via the aforementioned methods a heating is taking place to heat up the mold cavity quickly. Typically, conventional cooling is then applied to extract the heat as fast as possible after filling and packing.

A great number of studies have investigated the use of induction heating to obtain a very fast heating in the mold surface by applying an external inductor coil. S. C. Chen et al. [2–7] have investigated induction heating with experiments and simulations on weld lines and their strengths, micro-features with high aspect ratio, comparing with electrical heaters, and pulsed cooling. Overall conclusions were induction heating had faster heating, using multiturn coil gives better temperature uniformity and that induction heating does improve the filling of micro features/cavities and weld lines strength, as well as their visual appearance.

K. Park et al. [8–16] also investigated an external induction heater together with unconventional cooling methods such as compressed air, which was investigated on a cup design and a micro gear. The ribs on the gear were found to be better replicated with induction heating. Combinations of different magnetic and nonmagnetic materials were also investigated to localize the heating around micro features. Work on weld lines was also carried out, and again improved weldline quality was obtained. The authors also realized automatic induction heating with feedback temperature control and found the gap between the coil and mold to be an important factor. Optical properties were improved with the use of induction heating.

M. S. Huang et al. [17–22] have compared the performance of oil heating versus induction heating and found the latter to give best replication of micro structures. They also noticed that increasing the mold temperature above the phase transition temperature does not significantly improve the replication ability. They showed that using multiple coil layers can give a more uniform temperature field. It was also investigated how ferrite materials can improve the induction heating from the coil, and this is found to be an important factor for increasing the heating rate.

C. T. Huang et al. [23, 24] compared different heating methods such as rapid heat cycle using, e.g., steam, induction heating, and electrical heating and showed its influence on the flow with experiments and flow simulations in Moldex3D. They also looked at the warpage of the parts and obtained reasonable agreement.

Several other studies [25–31] included applications such as induction heating with nanoscale molding, using low thermal inertia tools, weldlines at microscale, using infrared heating equipment, and in general on the improvement of microscale features/products. In common for all research is that a high mold temperature does improve the overall product quality and helps remedy the above-mentioned problems.

Induction heating in injection molding is typically based on using an external inductor, usually placed on a moving arm, which heats up the mold surface when the mold is open. The idea in this work is to build in an integrated internal inductor below the cavity surface [32, 33]. This creates a simpler molding procedure, since there is no waiting time for a robot arm to enter and heat the surface, exit again and then close the

mold. It also gives the benefits of making the heating available in the packing phase. One drawback will be the mold redesign, and a new way of thinking when constructing the tool will be needed.

Simulation and modeling of induction heating in injection molding have been the topic of several research works, which are typically dealing with the simulation of the induction heating itself [2–4, 8, 9, 15, 25, 32, 34], while the effect of fluid flow is emulated by assuming an equivalent thermal boundary condition [11, 14]. In these papers, the magnetic properties are assumed linear, that is, a linear relation between the magnetic field and flux. Simulations of coupled induction heating and fluid flow have been conducted [10, 12, 15], in which the electromagnetic analysis and the mold filling simulation are coupled by imposing either an average constant thermal boundary condition or the actual transient thermal field from the induction simulation to the fluid flow simulation. This is done by mapping the thermal field from the electromagnetic solution to the flow solver to include the effect of the induction heating during filling of the cavity. Imposing the mapped actual transient thermal field was found to give the most realistic results. The work done in [10, 12, 15] also assume linear magnetic data, similarly to the previously mentioned papers. In [23, 24], the thermal field is modeled in the injection molding flow solver to directly calculate the effect of a heated mold.

The present work has adapted an integrated multiturn induction heating coil into an injection molding tool, together with a transparent glass window, so that the effect of induction heating can directly be captured by a high speed camera. In addition, thermocouples and pressure sensors are also installed in the mold and together with the high speed videos, comparison of the induction heating, and filling of the cavity can be performed to validate the simulation results.

The magnetic materials that have been used in this wo rk include magnetic tool steels, which had their B-H relation and its dependence on temperature characterized by the authors in [35], and in this work this is employed in a nonlinear axisymmetric model to find the effective linear magnetic permeability as presented by authors in [36]. This is transferred to a 3D induction heating model to find the transient thermal field of the mold cavity. This thermal field is then transferred to the flow solver, and the resulting flow simulations, both without and with induction heating, are then compared with the experimental filling flow results from the high speed camera and the sensors.

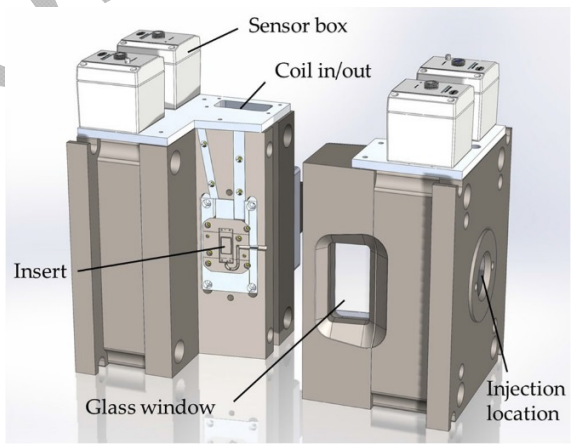

Fig. 1 Schematic overview of the two mold halves of the glass mold, showcasing the different parts

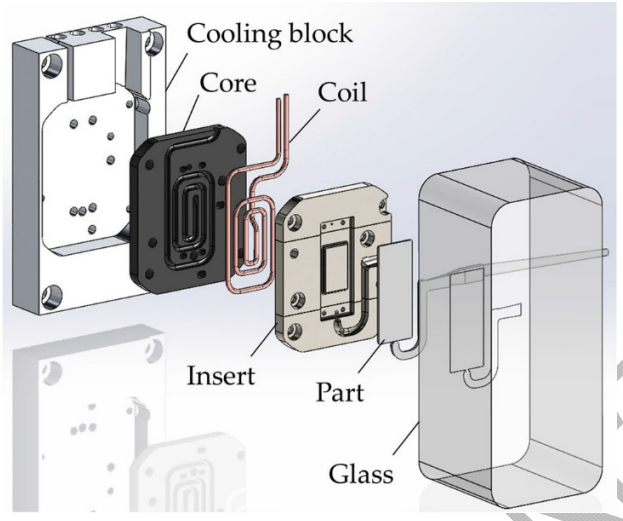

Fig. 2 Exploded view of the components around the glass and insert. The core, coil, and insert are put together and inserted into the mold block with the cooling channels

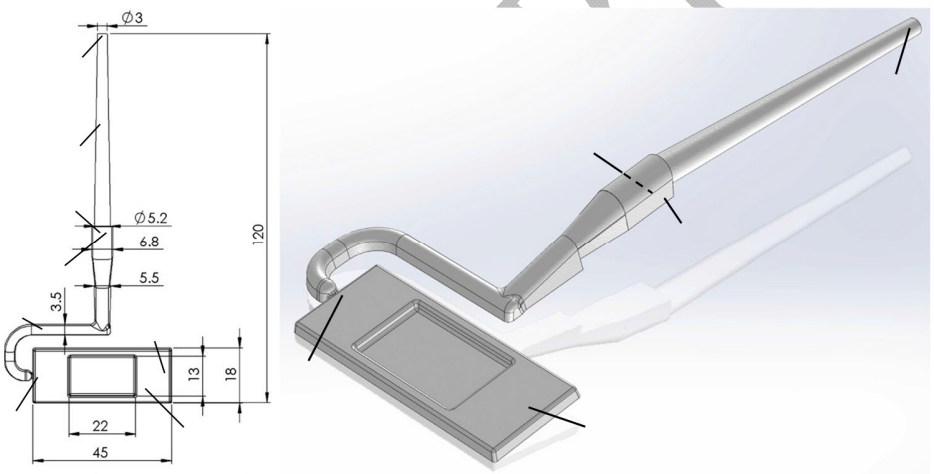

Fig. 3 The test part with an overall thickness of 2 mm, and a center section with thickness of 0.5 mm, noted with sensors location. P1 and P2 indicate the pressure sensors; T1, T2 and T3 indicate the thermocouples

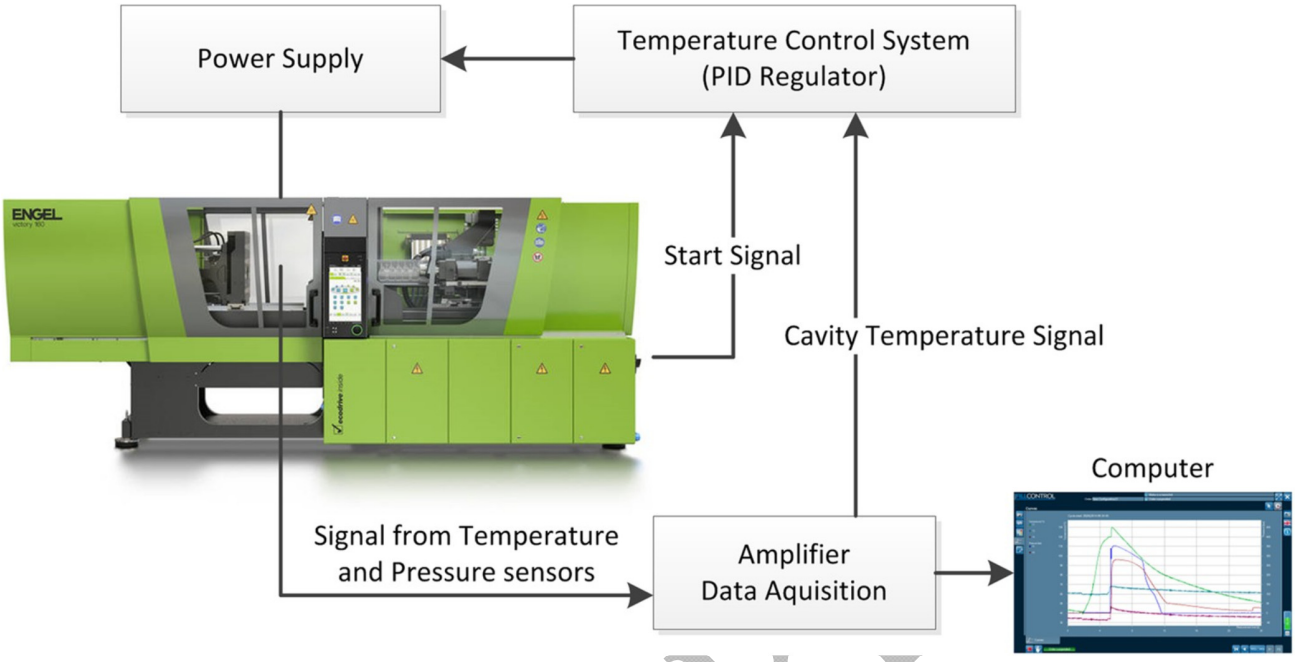

Fig. 4 Experimental setup with the coupling between the molding machine and the power supply

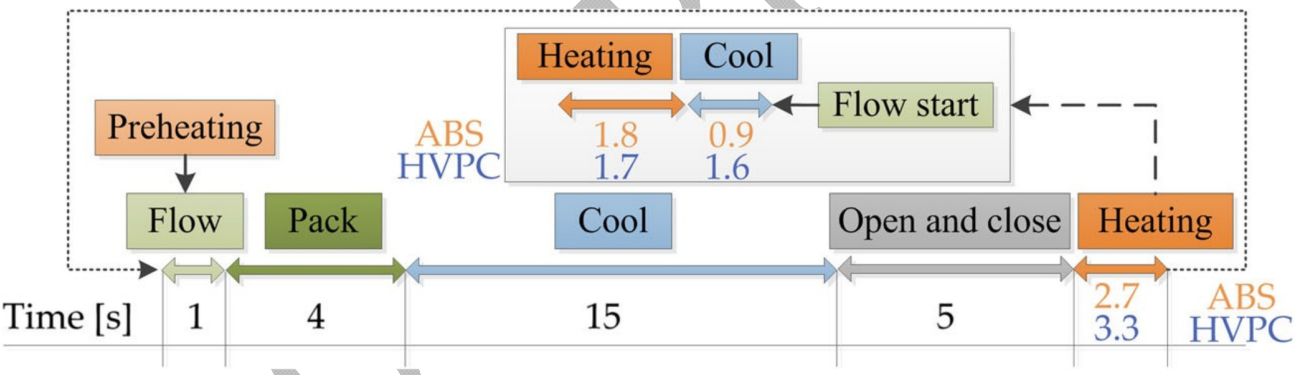

Fig. 5 Injection molding cycle used in the experiments. The preheating is only used in the simulation in order to quicken up the converge to the cyclic steady state solution

2 Induction heating simulation

2.1 Governing equations and implementation for the induction heating

The electromagnetic part of induction heating is governed by Maxwell's equations. Maxwell's equations can be combined in to a simpler form [37]:

$$\frac{1}{\mu}\nabla^2\bar{\mathbf{A}} - i\omega\sigma\bar{\mathbf{A}} = -\bar{\mathbf{J}}_s \qquad (1)$$

where **A** is the magnetic vector potential related to the magnetic flux by **B** = ∇ ×**A**, **J***s* is the source current density in the coil, $\omega = 2\pi f$ is the angular frequency (and f the frequency), σ is the electrical conductivity, and the overbar is denoting the peak value or the amplitude. The flux density is assumed to lie in the plane of the model (xy or zr), while the vector of electric current density **J** and the vector potential **A** are orthogonal to it. Only Jz and Az in planar or $J\theta$ and $A\theta$ in axisymmetric case are not equal to zero. As such, Eq. 1 is easily solved for the induction heating problem in the axisymmetric case in this work. It is solved using a Galerkin finite element method with linear triangular elements, in an in-house, self-developed simulation program written in Matlab [32, 36].
For solving Maxwell's equations in 3D, it is required to solve for more unknowns if Eq. 1 were to be solved, since **A** has three components in each node and is defined in the whole region, and as such it is computationally very demanding. To reduce the number of unknowns for eddy current problems, the time harmonic Maxwell's equations can be formulated as follows:

$$\frac{1}{\sigma}\nabla^2\bar{\mathbf{H}} - i\omega\mu\bar{\mathbf{H}} = 0 \tag{2}$$

$$\mu\nabla^2\bar{\varphi} = 0 \tag{3}$$

where **H** is the magnetic field and ϕ is the magnetic scalar potential (where **H** = ∇ϕ). Equation 2 is solved for conducting regions from source currents, and this is more computational heavy due to the fact that it is solving for a vector, and Eq. 3for non-conducting regions [38]. This is solved using the Ansys Maxwell3D software module which solves Eqs. 2 and 3 using tetrahedral edge elements. First, Eqs. 2 and 3 are combined, then **H** is forced to be continuous on the internal boundaries, producing a continuous field solution throughout the model, which is then solved for. A mesh sensitivity analysis is subsequently performed until a specified error criterion (in %) is met.

Due to the assumption that a time-harmonic varying source current is applied, the heat source term arising from eddy currents can be written as follows [39]:

$$\dot{Q} = \frac{1}{2\sigma}\left|\bar{\mathbf{J}}\right|^2 = \frac{1}{2\sigma}\bar{\mathbf{J}}\cdot\bar{\mathbf{J}}^* \tag{4}$$

where $\bar{\mathbf{J}}$ is found from the solution of Eq. 1 in the 2D case ($\bar{\mathbf{J}} = -i\omega\sigma\bar{\mathbf{A}}$) and the solution of Eqs. 2 and 3 in the 3D case ($\bar{\mathbf{J}} = \nabla\times\bar{\mathbf{H}}$).

For the calculations of the temperature distribution from the induction, the transient heat conduction equation is solved:

$$\rho c_p\frac{\partial T}{\partial t} = k\nabla^2 T + \dot{Q} \tag{5}$$

where T is the temperature, ρ is the density, cp is the specific heat capacity, k is the thermal conductivity, and $\dot{Q}$ is the heat source from Eq. 4.

The spatial part of the heat conduction equation (5) in axisymmetric coordinates is discretized in a similar way as in the electromagnetic axisymmetric FE model. The time derivative is discretized using an implicit Euler formulation with a time step of 0.1 s. For the 3D solution of Eq. 5, Ansys Transient Thermal using Mechanical APDL solver is used, which is coupled to the Ansys Maxwell3D through Ansys Workbench. A time step between 0.01 and 0.1 s is applied. In the case of the nonlinear magnetic permeability μ for the 2D axisymmetric calculations, the equations are solved using an iterative method [36, 40], with an analytical description of the anhysteretic B-H curve using the modified FrÃhlich equation:

$$B = \frac{H}{\alpha + \beta |H| + \gamma \sqrt{|H|}} + \mu_0 H \qquad (6)$$

Where α, β, and γ are material fitted parameters (which can be temperature dependent). They are found from the measured materials from [35], and the materials constants from [36]. The nonlinear material is approximated with a fictitious linear material that has a constant relative permeability, which is unknown, called μ^f_r where f denotes the fictitious material. The linear fictitious material should have the same average heat density loss as the nonlinear material, in every point. The linear fictitious permeability is found by [40]:

$$\mu^f_{ri} = \frac{w_{1i} + w_{2i}}{\mu_0 \left(H^f_{mi}\right)^2} \qquad (7)$$

where w_{1i} and w_{2i} are the magnetic co-energy density of the material. w_{1i} is related to the actual B-H curve by $w_{1i} = \int_0^{H^f_{mi}} B \mathrm{d}H$, and w_{2i} is related to the average value of the slope $\frac{dB}{dH}$ during a quarter of a period T by $w_{2i} = \frac{1}{2} B_{mi} H^f_{mi}$. H^f_{mi} is the maximum value of the magnetic field intensity in the fictitious material.

The magnetic co-energy density is evaluated in [36] together with detailed explanation of the iteration procedure.

Table 1 Electromagnetic and thermal properties used for the different materials

Material	Initial relative permea-bility (-)	Electrical conductivity (S/m)	Thermal conductivity (W/mK)	Density (kg/m3)	Specific heat capacity (J/kgK)
Air	1	0	0.026	1.1614	1007
Aluminum	1	3.8e7	237.5	2689	951
Coil insulation	1	0	0.4	930	2300
Glass	1	0	1.4	2500	750
Copper	1	5.8e7	400	8933	385
Orvar	75[a]	1.64e6	28	7750	460
Somaloy	500[a]	3.85e3	7.5	7300	447
Water	1	2e-4	0.6	1000	4180

[a]Estimated effective linear value since it is non-linear

Table 2 Summary of injection molding processing condition for ABS and HVPC

Polymer	Injection time t_{inj} (s)	Packing time t_p (s)	Packing pressure P_p (MPa)	Mold temp, no indc. T_m (°C)	Mold temp with indc. at T_3 (°C)
ABS	1	4	40	22	120
HVPC	1	4	50 stepping down to 35	90	165

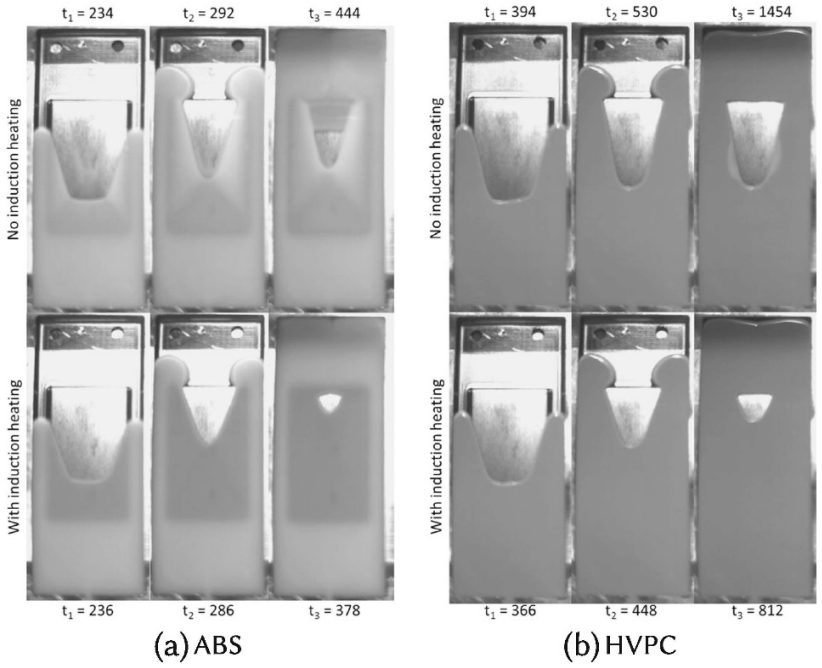

Fig. 6 Flow patterns recorded with the high speed camera at the corresponding injection time (in ms) from the melt first enters high speed video frame (t1, t2, t3) without induction heating (top) and with induction heating (bottom) for the two materials

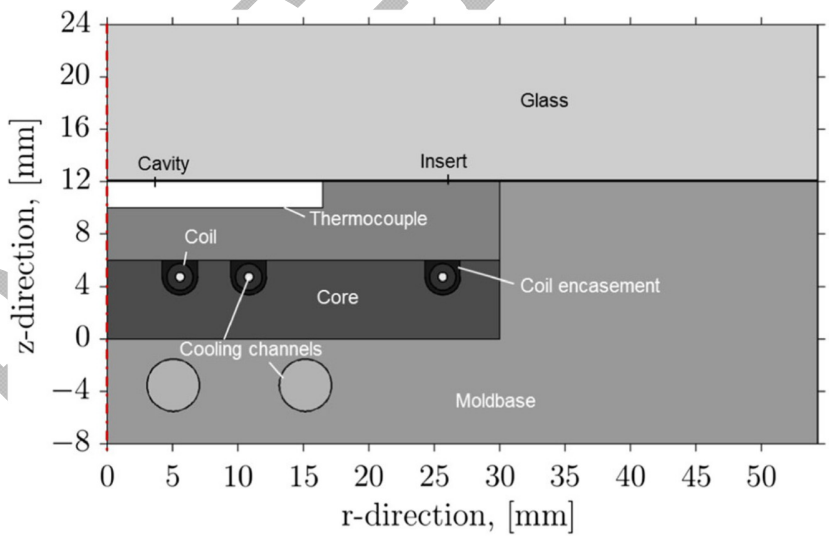

Fig. 7 Schematic overview of the sections in the axisymmetric numerical model of the flat Somaloy flux concentrator

2.2 *Governing equations for the injection molding flow*

For the flow simulations, the principle of conservation of mass, momentum, and energy is used for the governing equations:

$$\frac{\partial p}{\partial t} + \nabla \cdot \rho \mathbf{u} = 0 \tag{8}$$

$$\frac{\partial}{\partial t}(\rho \mathbf{u}) + \nabla \cdot (\rho \mathbf{u}\mathbf{u} - \boldsymbol{\sigma}) = \rho \mathbf{g} \tag{9}$$

$$\boldsymbol{\sigma} = -p\mathbf{I} + \eta\left(\nabla \mathbf{u} + \nabla \mathbf{u}^T\right) \tag{10}$$

$$\rho c_p \left(\frac{\partial T}{\partial t} + \mathbf{u} \cdot \nabla T\right) = \nabla \cdot (k \nabla T) + \Phi \tag{11}$$

$$\Phi = \eta \dot{\gamma}_{eq}^2 + \Delta \dot{H} \tag{12}$$

where ρ is the density, $\mathbf{u}$ is the velocity component, p is the pressure, σ is the total stress tensor, $\dot{\gamma}$ is the shear rate, $\mathbf{g}$ is the body force, c_p is the specific heat, k is the thermal conductivity, $\Delta \dot{H}$ is the heat released under solidification, and η is the viscosity taken as the generalized WLF-Cross viscosity model:

$$\eta = \frac{\eta_0}{1 + \left(\frac{\eta_0 \dot{\gamma}}{\tau^*}\right)^{1-n}} \tag{13}$$

where n is a power-law constant and τ^* is a transition stress. η_0 is a zero-shear rate viscosity represented by a WLF-type model to take into account the temperature and pressure effects:

$$\eta_0 = D_1 exp\left(\frac{-A_1 (T - T_c)}{A_2 + (T - T_c)}\right) \tag{14}$$

where A_1, A_2, and D_1 are material constants, and T_c is taken as the glass transition temperature which can vary with the pressure through D_3:

$$T_C = D_2 + D_3 P \tag{15}$$

For tracking the fluid flow front, a level set method is employed:

$$\frac{\partial f}{\partial t} + \nabla \cdot (\mathbf{u} f) = 0 \tag{16}$$

Where f is the volume fraction: f = 0 is the air phase, and f = 1 is the polymer melt phase. The melt front is tracked by the elements with 0 < f < 1. The equations are solved numerically with a finite volume scheme using a 3D unstructured boundary layer mesh (see Fig. 16 for the used mesh). For the purpose of this study, the commercially available software Moldex3D Solid R13 was employed.

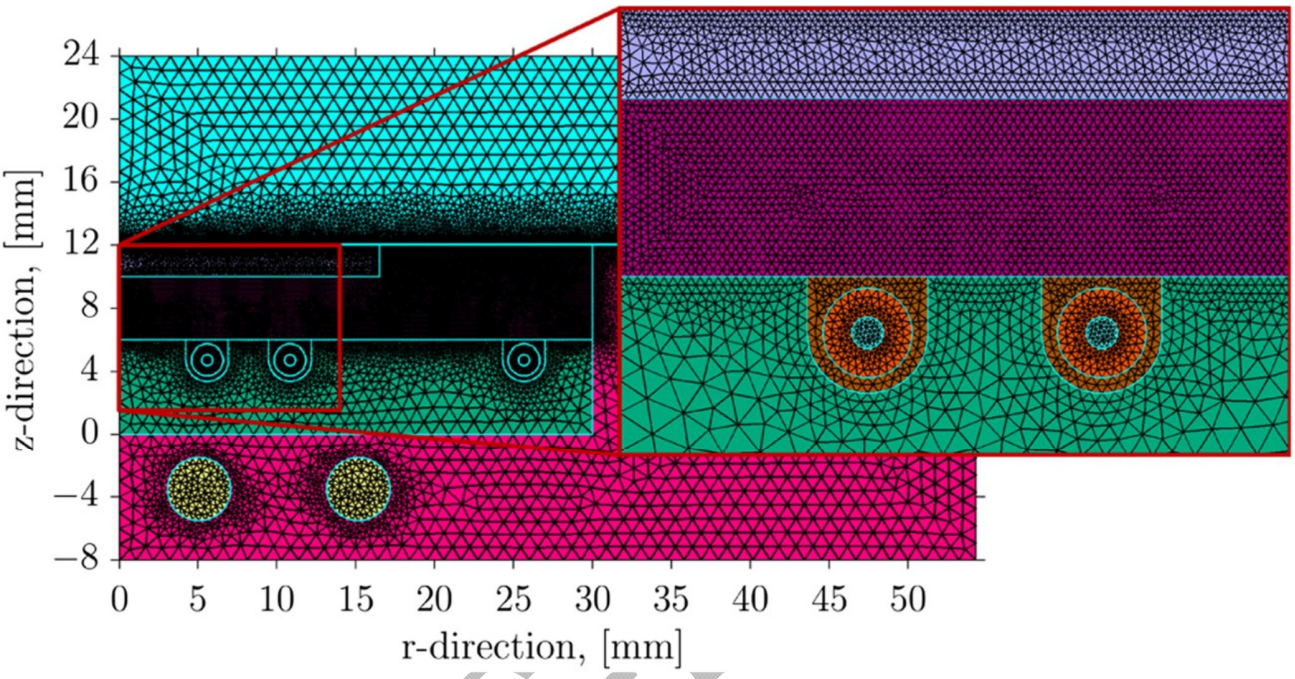

Fig. 8 Mesh of the mold with the Somaloy flux concentrator and coil. The total number of elements is 29,600 with 14,908 nodes. The mesh size in the cavity is 0.2 mm which is smaller than the skin depth of 0.3 mm

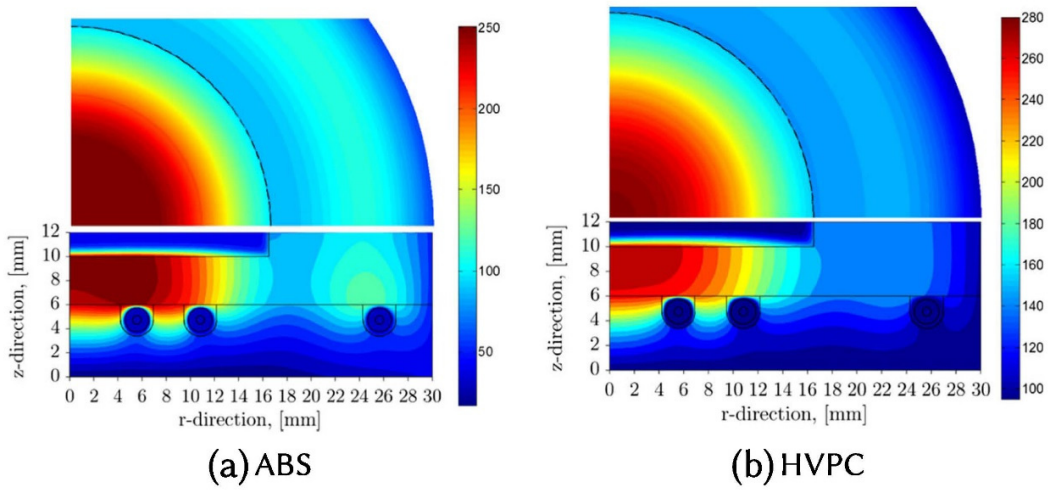

Fig. 9 Simulation at the start of injection, from the non-linear model. Top: the cavity surface; bottom: inductor cross section. (a) ABS (b) HVPC

3 Experimental method

3.1 Structure of the mold

An induction coil was installed in a special mold with a glass window, see Fig. 1. This was introduced in order to compare the induction heating effect on the flow and to compare the results with simulations. The injection plane is perpendicular to the opening and closing plane, in order for the glass window to easily be visible from the side. It is turned 8° to avoid any breakage of the glass during opening and closing of the mold. The different components installed are shown in Figs.1 and 2.

The glass is installed in the stationary mold half, whereas in the moving half, the insert which has the cavity for the part geometry is installed. Behind the insert, the coil which carries the current that induces the magnetic field is positioned. The coil is inserted into a core, which concentrates the magnetic field into the insert. These components are placed in an aluminum block with water cooling channels. The magnetic flux concentrator is made of a soft magnetic composite which is easy to machine by milling, since normal core material is too brittle for that. The ejector system is located behind the cooling block.

3.2 Sensors and placement

In addition to the induction heating system and glass window, three thermocouples and two pressure sensors are installed. The thermocouples provide multiple information: they show what the temperature is in the mold insert, they reveal at what time the melt passes the location due to a sudden change in the temperature, and acts as a feedback for the proportional-integral-derivative (PID) controller. The pressure sensors are used to validate the simulations, and to see how the pressure, is affected by the induction heating. See Fig. 3 for the sensors locations in the inlet and part.

The coupling between the different components in the induction heated injection molding tool can be seen in Fig. 4. A power supply (Minac 12/18 from EFM Induction a/s) is connected to the induction coil, through a transformer. The power supply gets a signal from the injection molding machine before injection and the power supply delivers 220 A for a defined amount of time. The PID regulator is given a specified temperature as a target temperature to be reached in the set time. It gives 220 A at a frequency of 22 kHz until the target temperature is almost reached and then it lowers the current and stops. It uses the thermocouple installed in the insert (T3 in Fig. 3) as this indicates the cavity temperature. The sensor signals are acquired by an amplifier and stored on a computer, where it is also visualized as the process runs.

The injection molding process cycle can be seen in Fig. 5. After the mold closes, the start signal for the PID regulator is given, and the power supply produces the currents in the coil. It stops when the specified time is reached, and a short cooling phase is commenced, where the heat is distributed more evenly over the cavity surface, as the heat during induction is mainly concentrated on the coil side of the insert. Then the injection begins, followed by the packing and cooling phases. This procedure was repeated until a cyclic steady state was reached, typically corresponding to between 10 and 15 shots.

3.3 Materials

Two polymer grades where used in this work included acrylonitrile butadiene styrene (ABS) and a high viscosity polycarbonate (HVPC). It is the objective to reach their no flow temperature Tno−flow in the thin section in the middle of the part, see Fig. 3. This is usually close to the glass transition temperature Tg which is 94 °C for ABS and 150 °C for HVPC. The Tno−flow is around 111 °C for ABS and 160 °C for HVPC, so the target temperature for the thermocouple should be above this temperature, to ensure a higher temperature than the no flow temperature. Also, since it is a flat coil which covers the area of the cavity, the temperatures will be higher in the center due to heat conduction, as the heat tends to concentrate in that area [36].

The materials for the mold and heating system (see Table 1) are chosen in this work based on their magnetic permeability, electrical conductivity, and thermal conductivity to be able to heat one side of the mold cavity, since the other half consists of glass. The coil is made of copper, with an electrical insulated material around it, consisting of both Nomex paper and a shrink tube. The flux concentrator is a material from Hgans called Somaloy Prototyping Material, and it consists of tiny nano-coated iron particles that make the surface of each particle insulated. The Somaloy is therefore magnetic with low electrical conductivity, and this promotes the magnetic field in front of it, without having noticeable resistive losses. Moreover, it has a lower thermal conductivity compared to the mold material, so it slows down the heat conduction from the insert. The insert is made of the tool steel Orvar Supreme from Uddeholm, which is both magnetic and electrically conductive, and since the Somaloy has a lower thermal conductivity, the insert itself can be thought of as the thermal mass to be heated.

3.4 Experimental comparison using process data and high speed video

The injection molding experiments (see Table 2) were carried out on an Engel Victory 60 with a 35-mm diameter screw, with an injection ram speed of 10 mm/s for ABS and 12 mm/s for HVPC, to reach a total filling time of 1 s, including ram acceleration and injection until the packing phase. Due to the ram size, the compressibility of the molten polymer in front of the nozzle had an effect on the filling time, together with the ram acceleration. This resulted in the cavity itself being filled in about 470 ms, where approximately 260 ms was from the packing phase for the ABS. For the HVPC case, a short shot is obtained, so the time from the gate to the packing phase is around 390 ms (210 ms for ABS). The packing pressure used for ABS was 40 MPa in 4 s, and 50 MPa stepping down to 35 MPa for the HVPC.

The flow pattern without and with induction heating can be compared in Fig. 6. The filling with no induction heating for both materials shows a filling pattern where the two thick sides start to fill faster than the thin middle section due to its resistance to the flow. At some point, the flow stops entirely in the thin section, as the frozen layer becomes so thick that it blocks the polymer melt, and the flow front is solidified. Since the ABS material has higher flowability, the middle section gets filled from the top, with material flowing in the sides and back down into the 'V' section. This gives a poor surface finish, and almost no strength, since it could easily be broken by hand force. The HVPC instead creates a short shot, as the middle section cannot be filled, due to the material's higher viscosity, and solidifies before the melt can reach the 'V' section from the top. HVPC even has problems filling out the corners in the top.

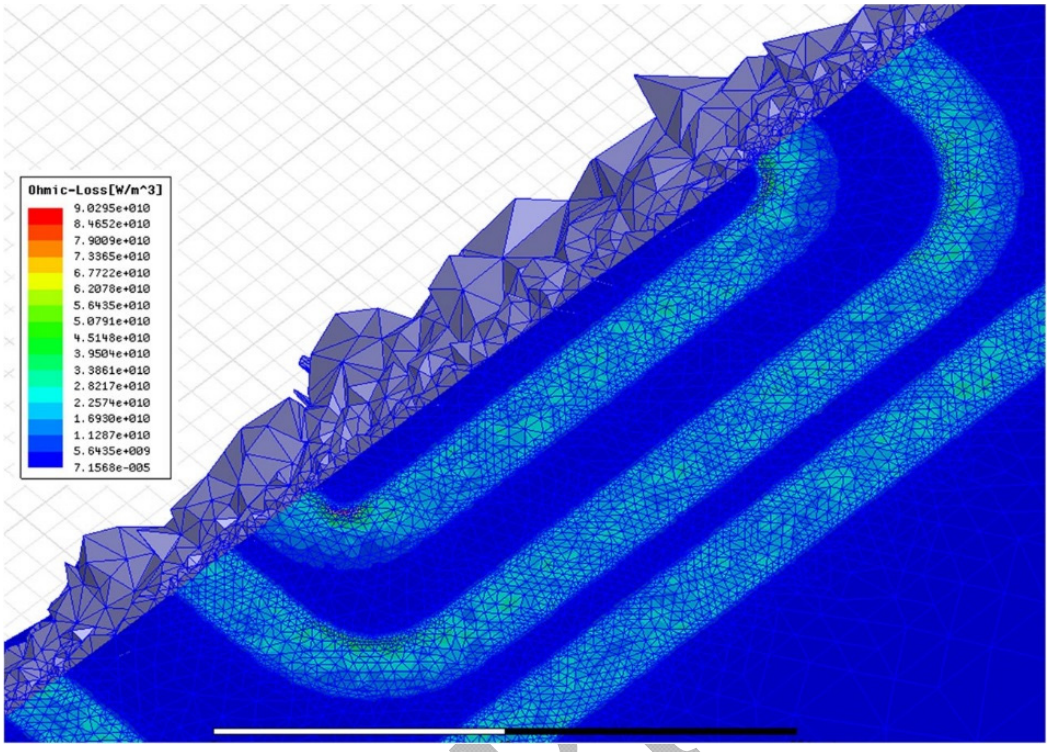

Fig. 11 Joule heat distribution and the mesh generated by Maxwell3D

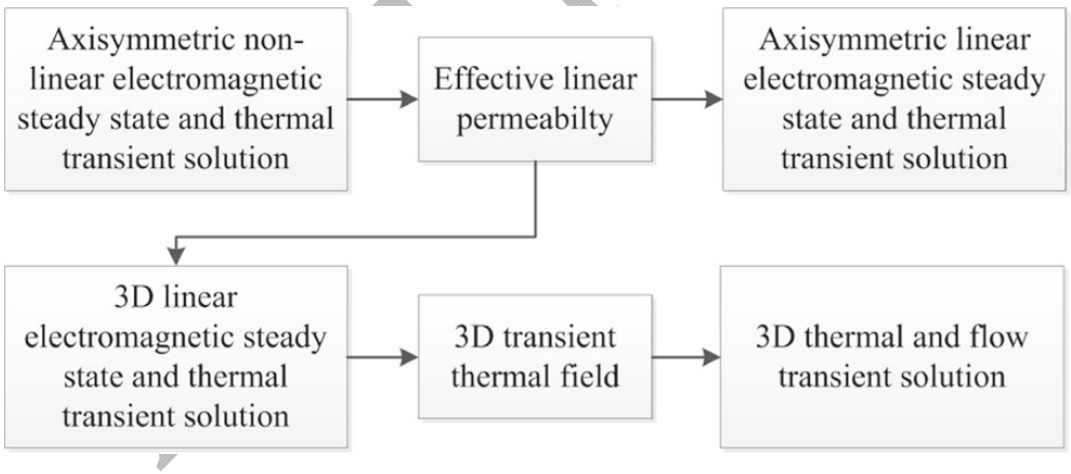

Fig. 10 Flow chart of the different model couplings considering the nonlinear magnetic material properties to find and effective linear permeability for the 3D analysis and transferring the thermal field to the flow simulation

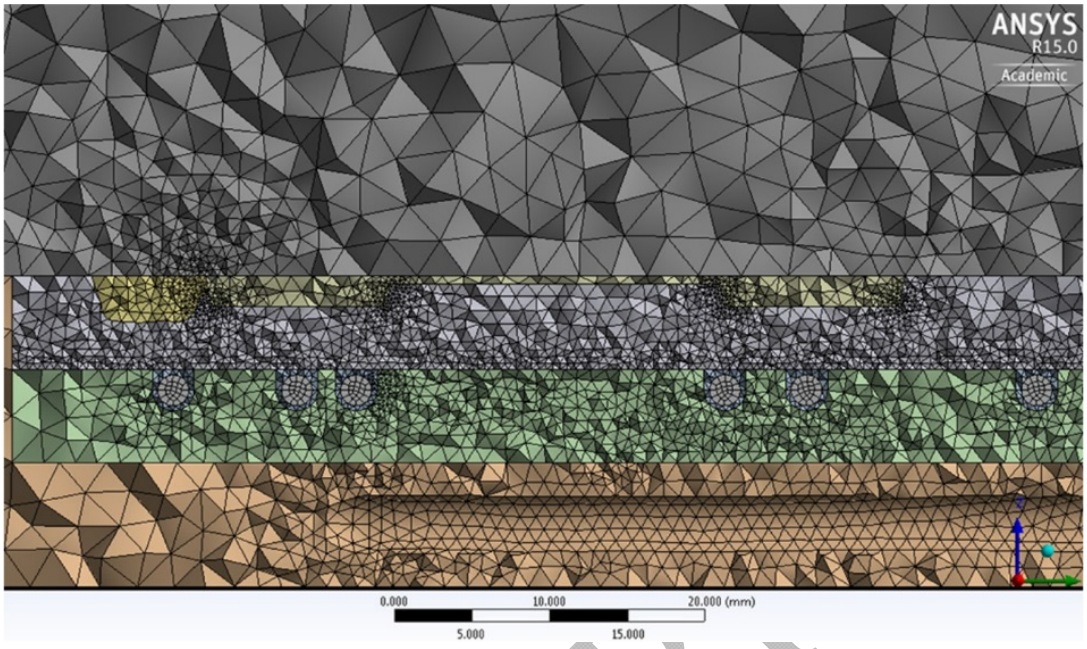

Fig. 12 Three dimensional mesh for the transient thermal analysis

4 Computational setup and results

4.1 Axisymmetric case

4.1.1 Setup

The real setup is indeed not an axisymmetric geometry, as seen in Fig. 2, but in order to utilize the nonlinear permeability of the materials characterized by authors [35], the self-developed simulation program has been utilized to find an effective linear permeability that can be used in the linear 3D simulation. This has proven to be an effective way to estimate a linear permeability of a nonlinear problem [36].

The axisymmetric setup assumes that the top of the insert (in Fig. 2) is axisymmetric around the top of the middle section, that is the extruded feature in the center of the cavity. In this setup, three coil windings are modeled, and the location of the thermocouple T3 from the experiments is included. The different sections are shown in Fig. 7.

The boundary conditions imposed for the electromagnetic analysis are a vanishing magnetic field at the outer boundary, as well as at the axis of rotation. The induced current is 220 A at a frequency of 22 kHz. The boundaries for the thermal calculations are described via a heat transfer coefficient between the surroundings and the mold material as

$$-k\frac{\partial T}{\partial n} = h\,(T - T_\infty) \qquad (17)$$

where h is the heat transfer coefficient which is set to 1000 W/m²K for the metal contact sections (south and east boundary), and 10 W/m²K for the boundary to the air (north boundary), and $T\infty$ is the temperature of the mold material or the room temperature, respectively. The axis of rotation is defined as an adiabatic boundary. Between the two mold halves, that is at y = 12 mm, the heat flux will be lower due to a potential air gap of 0.1 mm between the mold half with the insert and the glass, giving an effective heat transfer coefficient of 260 W/m²K. The temperature in the cooling channels is set to 17 °C. The initial temperature is set to room temperature of 25 °C, and the heating is turned on for 1.7/1.8 s for ABS/HVPC (see Fig. 5) and cooling (or simply conduction) for 0.9/1.6 s before the melt flow enters the cavity. This is assumed to happen instantaneously as the time scale of the filling of the cavity is in the order of hundreds of milliseconds, and the cavity section is an imposed temperature field of the melt temperature. The packing and cooling phase is then 19 s in total and followed by an opening and closing of the mold for 5 s.

The mesh has 29,600 elements and 14,908 nodes and is shown in Fig. 8. As seen, it is necessary to have a fine mesh in the magnetic material due to the well-known skin depth (or penetration depth) [37, 39], which is derived from Maxwell's equations. This quantity is defined as the distance for which the amplitude of a plane wave decreases by a factor of e^{-1} = 0.368:

$$\delta = \frac{1}{\sqrt{\pi f \mu \sigma}} \tag{18}$$

where f is the frequency, μ is the magnetic permeability, and σ is the electrical conductivity. This means that 63.2% of the magnetic field and currents will run within this distance, hence in order to resolve the solution properly it is normally recommended to have the equivalent of at least three skin depths of fine mesh elements.

4.1.2 Results

The temperature distribution on the mold cavity is shown for both ABS and HVPC Fig. 9 in the top, at the point of where the filling begins. A cross-section view is shown below. It is evident that the heat has spread out via conduction towards the center and surface, due to the heat being stored in the insert and almost insulated at the cavity surface, while cooling down from the backside where the cooling channels are.

While the temperature signal from T3 is at a maximum temperature before the melt hits of around 125 °C, it can also be seen that it is more hot towards the center, which is the flat middle section of 0.5 mm.

The temperature curves compared with the measurement from the thermocouple T3 are shown later in Section 4.3.2 (Fig. 22 for ABS and in Fig. 23 for HVPC), using the nonlinear temperature dependent permeability. Even though the geometry is not entirely axisymmetric in the experimental setup, the simulation seems to give a very reasonable agreement with the experiment.

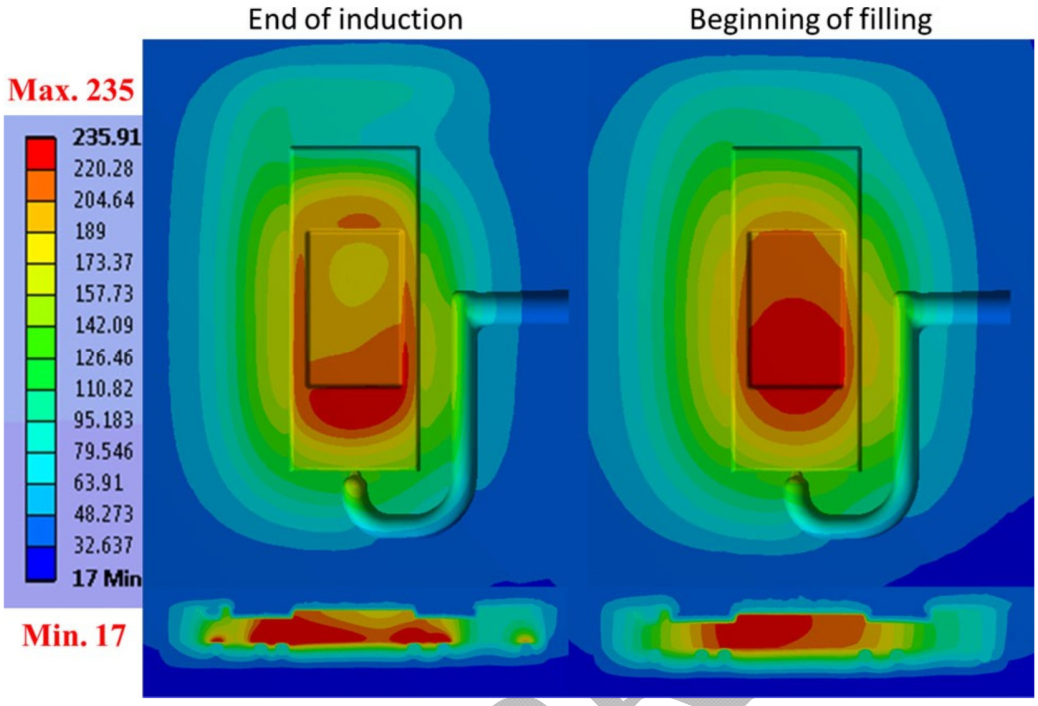

Fig. 13 ABS case after 1.8 s of induction heating to the right, and after induction is turned off in 0.9 s, before the filling starts

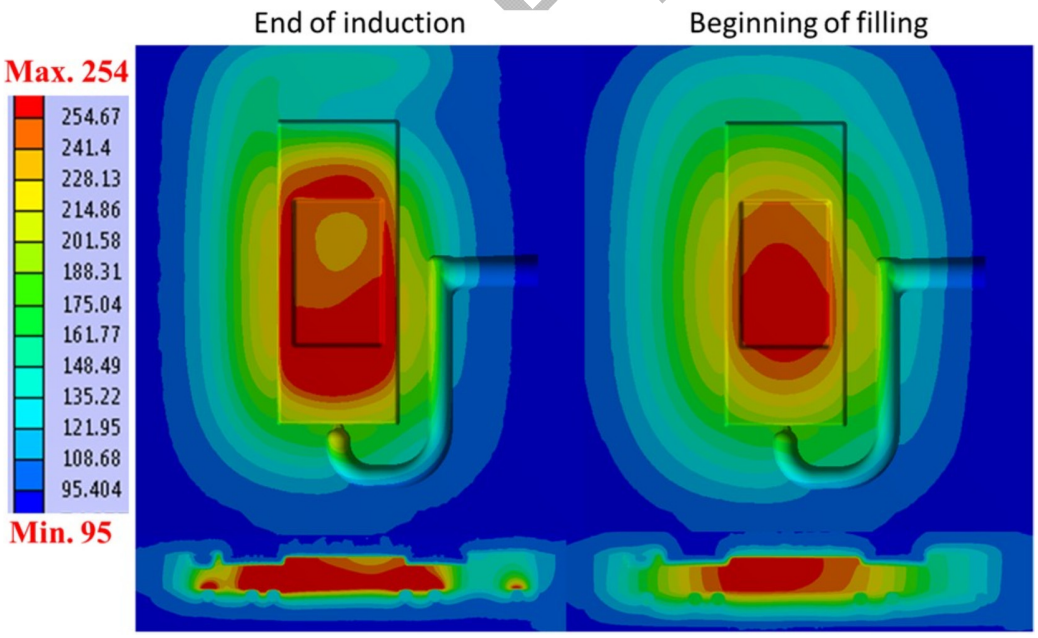

Fig. 14 HVPC case after 1.7 s of induction heating to the right, and after induction is turned off in 1.6 s, before the filling starts

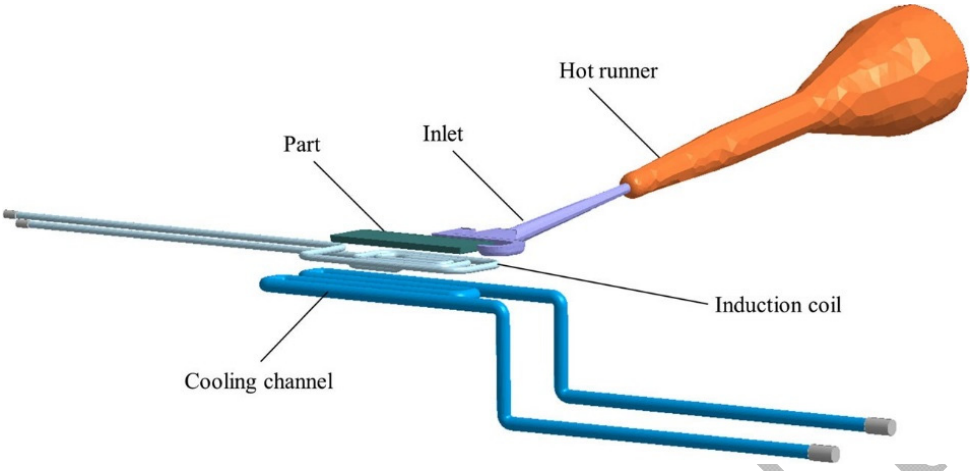

Fig. 15 Components in the flow simulation, except the glass and moldbase

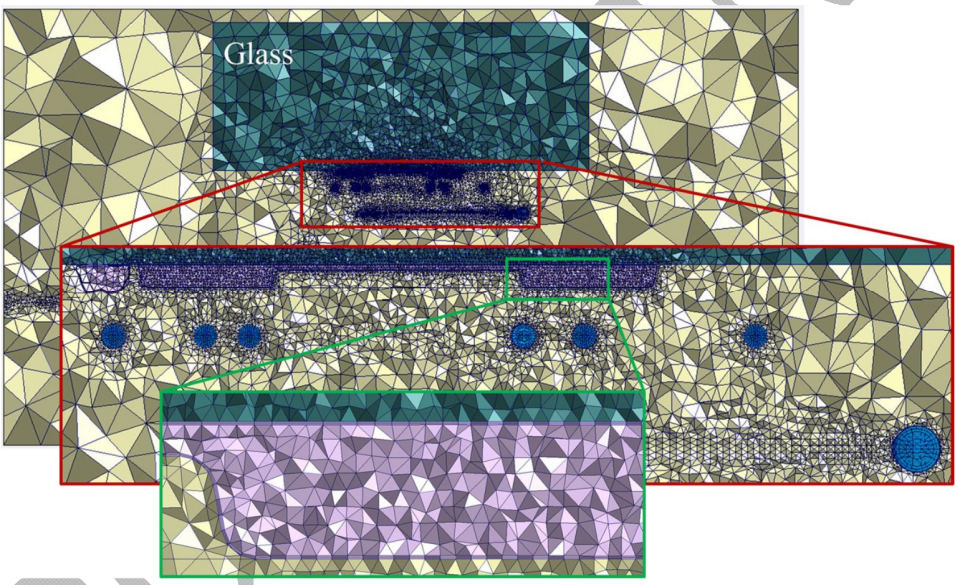

Fig. 16 Total number of elements in the model is 2.6 million, where 735.497 of the elements is in the part

4.2 Three-dimensional case

4.2.1 Setup

To obtain the temperature distribution on the mold cavity surface, a three dimensional analysis has been performed. Since most 3D solvers do not support nonlinear permeability for harmonic analysis, a linear effective permeability has been estimated from the nonlinear axisymmetric code as described in [36]. When the linear electromagnetic 3D analysis has computed the Joule heating, it is subsequently transferred to a 3D transient thermal analysis (Fig. 10). For the electromagnetic analysis in Maxwell3D, it took around ten

iterations to update and refine the mesh, so the energy change is below 1 % (that is the energy difference from last iteration). The total number of tetrahedrons was approx. 700,000, with most of the elements concentrated in the cavity surface as seen in Fig. 11. The Joule heat source term for the heat conduction equation is also shown in Fig. 11, and integrating over the insert volume, the generated power is 3800 W. This amount of generated power should provide an average temperature increase (assuming it is evenly distributed and the insert has adiabatic boundaries using $P_w = mc_p \cdot (Tf - Tin)/t$) from 45 to 132 °C after 1.8 s for the ABS case and from 95 to 177 °C after 1.7 s for the HVPC case. However, the temperature field is of course not evenly distributed as we saw from the axisymmetric case, it will be concentrated on the surface close to the coil, and then it will start to diffuse into the rest of the insert. There will also be a heat conducted away from the insert, so the uniform assumption with adiabatic boundaries is definitely an overestimation. The thermal analysis is setup similarly to the axisymmetric case, and the mesh of the different components can be seen in Fig. 12. The Joule heat from the Maxwell3D analysis is mapped to the mesh in the transient thermal analysis.

4.2.2 Results

In Figs. 13 and 14, the temperature distribution can be seen after 1.8/1.7 s, and the highest temperatures are concentrated in the lower part of the insert seen in the cross section. After the short conduction with no heat generation of 0.9/1.6 s, the highest temperatures are concentrated towards the center and the top of the insert. The temperature at the thermocouple T3 can also be seen in the later Section 4.3.2 (Figs. 22 and 23). The distribution is very similar for both materials, but the level of the temperature is different. Also, the temperature range over or close to the cavity surface area is above the desired no flow temperature for both cases, as the range is from around 110–200 °C in the ABS case and 155–250 °C in the HVPC case.

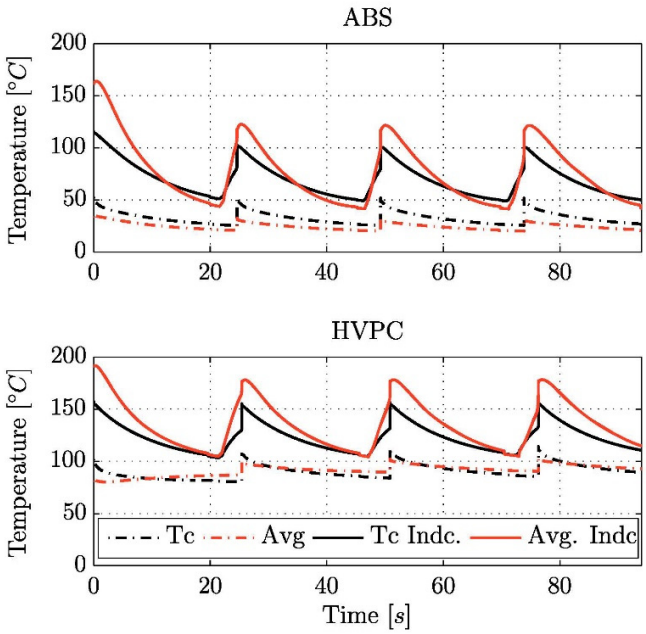

Fig. 17 Thermal cycles computed for the injection molding tool to be used in the flow calculation

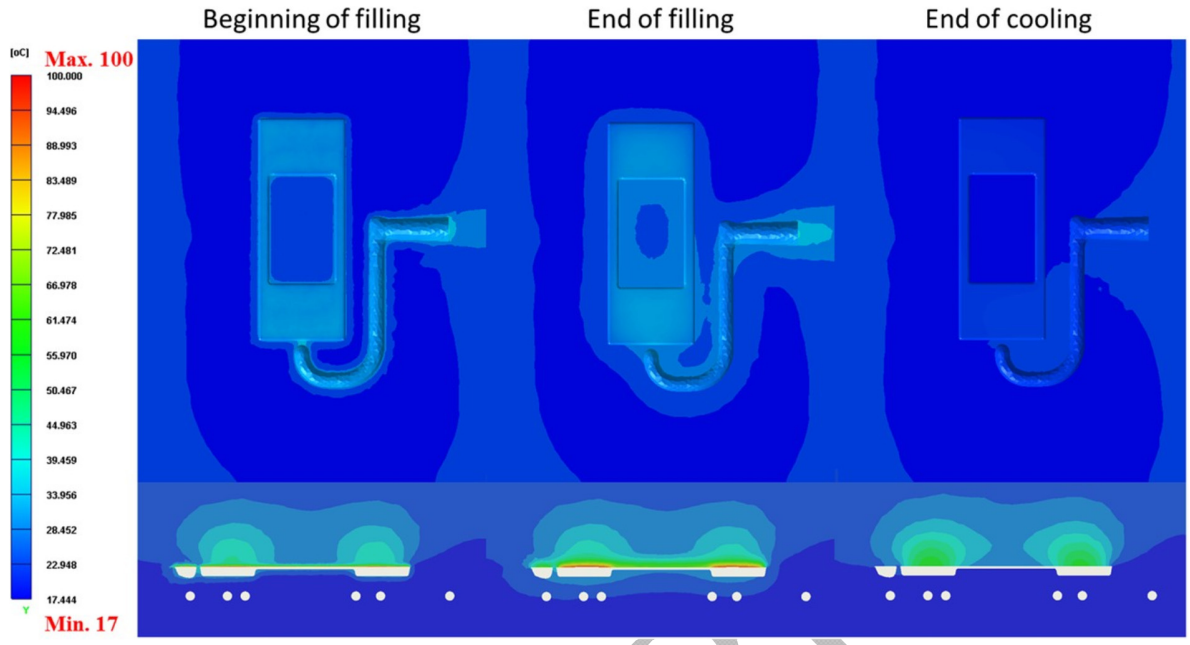

Fig. 18 ABS case from the Moldex3D simulation with no induction heating. Beginning of fill to the right, in the middle after the cavity is filled and to the right at the end of cool after 15 s

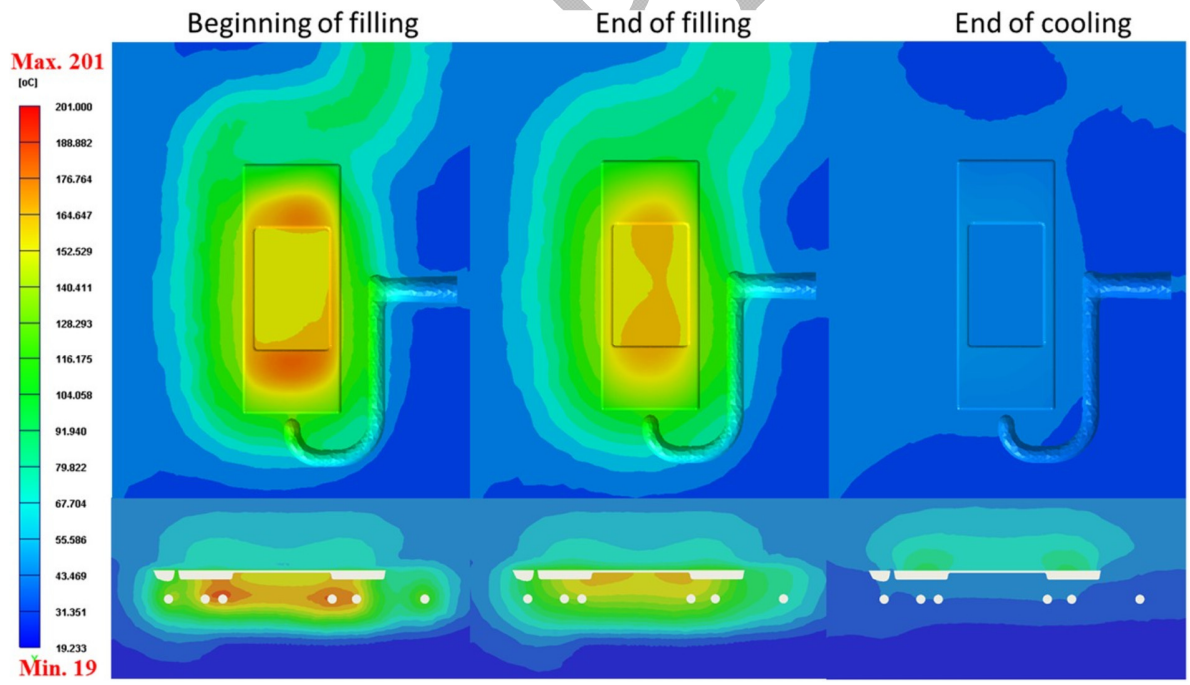

Fig. 19 ABS case from the Moldex3D simulation with induction heating. Beginning of fill to the right, in the middle after the cavity is filled and to the right at the end of cool after 15 s

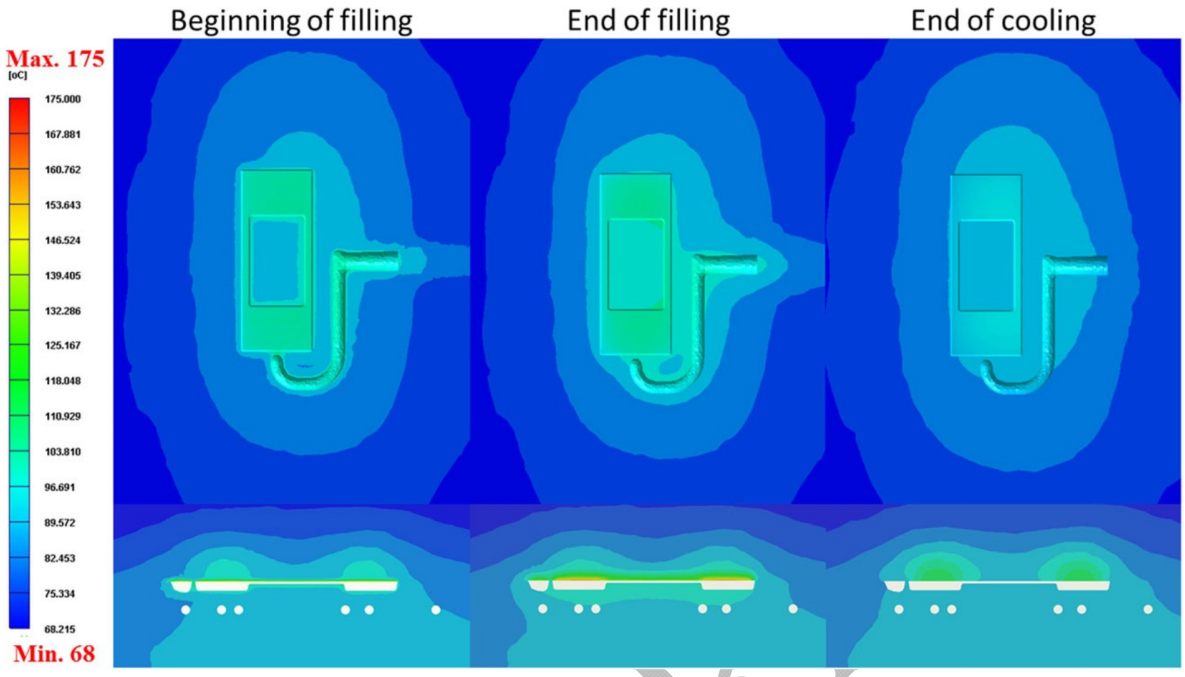

Fig. 20 HVPC case from the Moldex3D simulation with no induction heating. Beginning of fill to the right, in the middle after the cavity is filled and to the right at the end of cool after 15 s

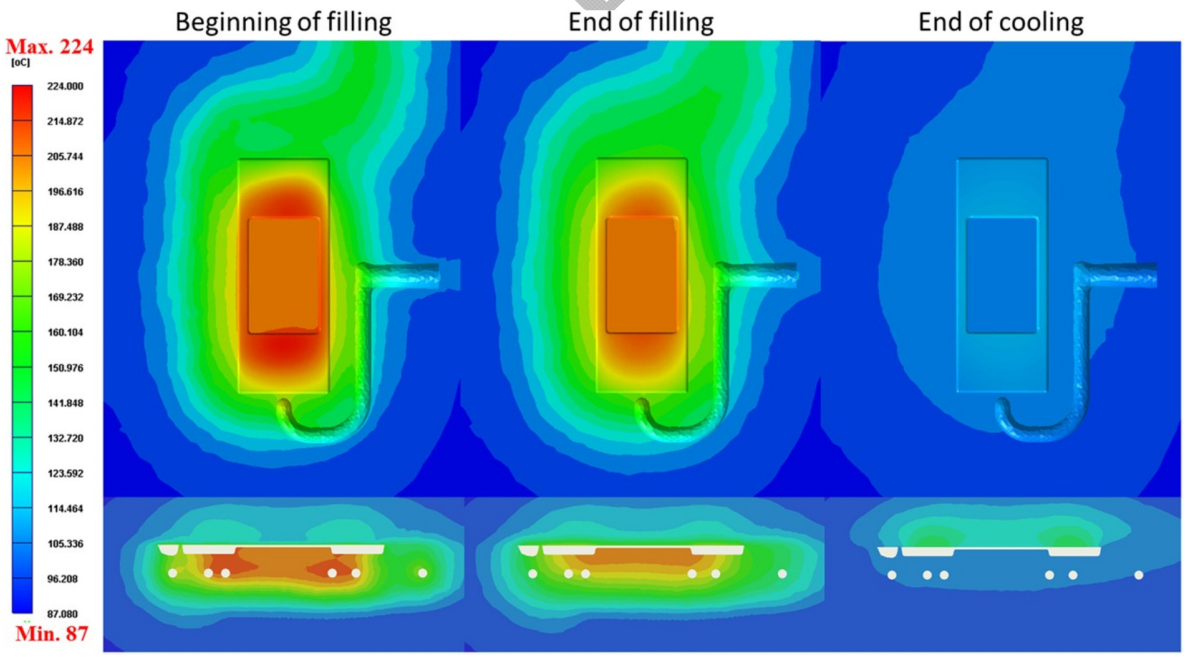

Fig. 21 HVPC case from the Moldex3D simulation with induction heating. Beginning of fill to the right, in the middle after the cavity is filled and to the right at the end of cool after 15 s

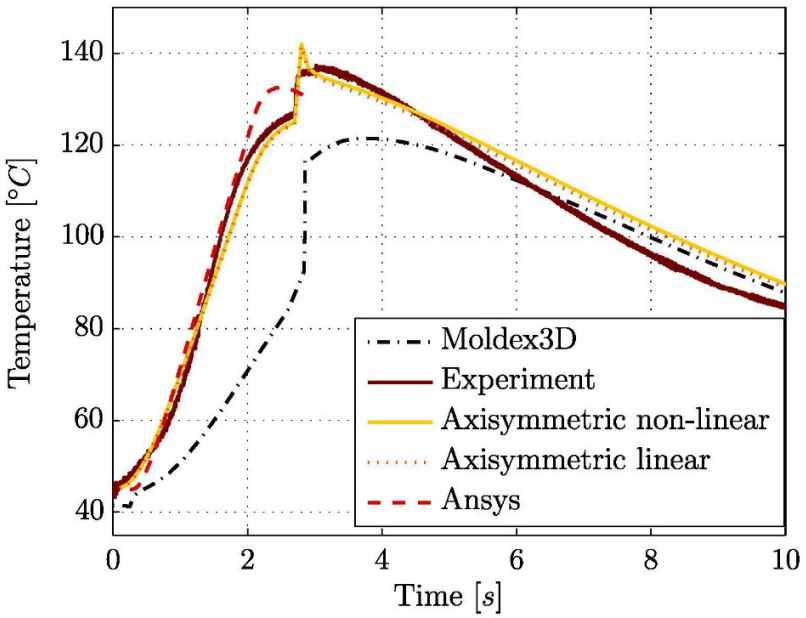

Fig. 22 Temperature comparison at thermocouple location for ABS

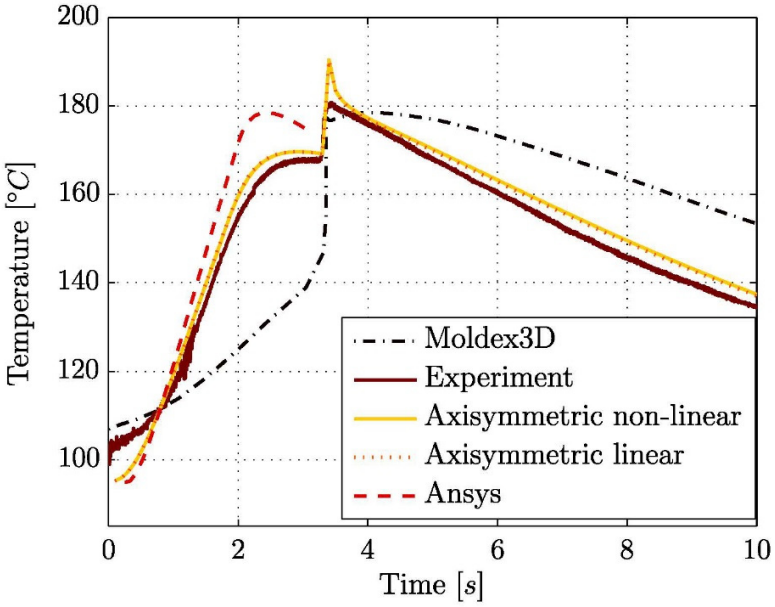

Fig. 23 Temperature comparison at thermocouple location for HVPC

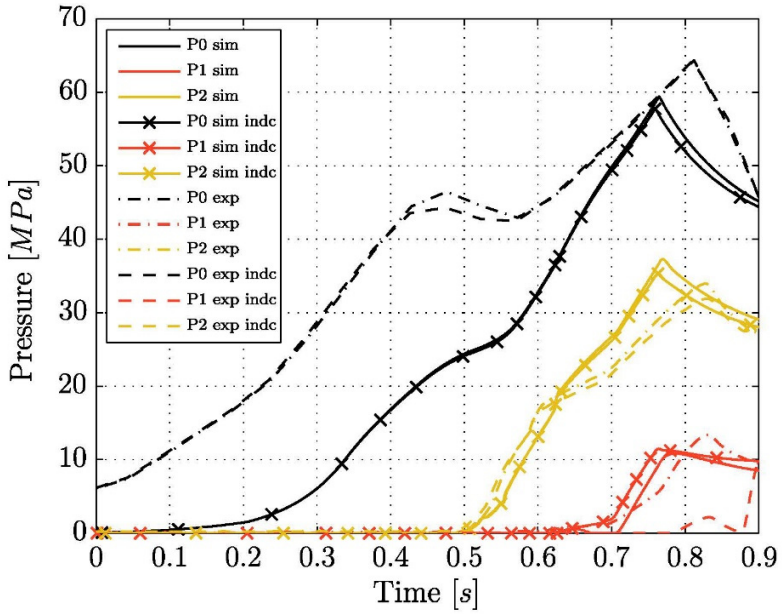

Fig. 24 Pressure comparison of experiments and simulation with and without induction heating for ABS

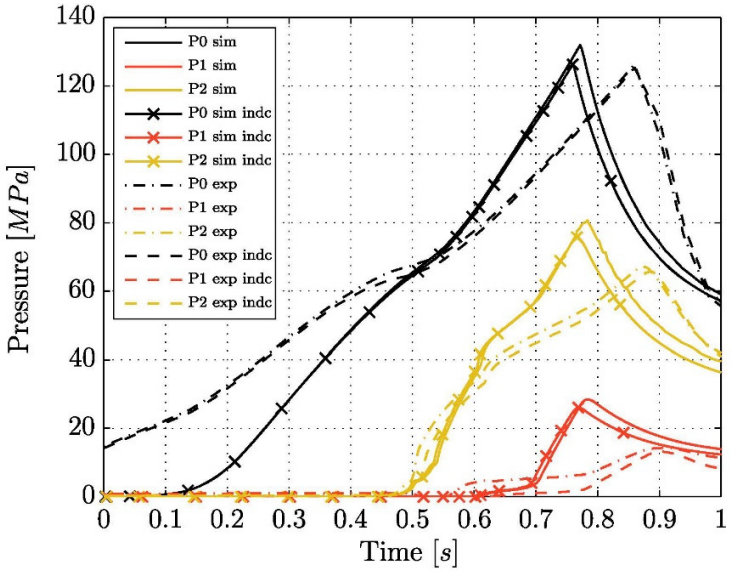

Fig. 25 Pressure comparison of experiments and simulation with and without induction heating for HVPC

4.3 Injection molding flow simulation

4.3.1 Setup

The different components of the flow simulation can be seen in Fig. 15 except from the glass and moldbase, which can be seen in the mesh in Fig. 16. The induction coil is here inserted as a cooling channel, which uses steam, since induction heating is not directly supported in Moldex3D [23, 24]. The steam temperature is set to 250 °C for 3 s, and then 45 °C when the induction heating is turned off for ABS. Similarly for HVCP 250 °C for 4 s to emulate the induction and then 95 °C when the induction heating is turned off. Before the injection molding thermal cycles were calculates, a preheating of the mold was executed for 6/7 s (ABS/HVPC) with induction on, see Fig. 5. This temperature was used as initial temperature for the thermal cycles.

The injection flow rate was specified in order for the filling (i.e., injection) time to be close to 1 s. This target was achieved by adjusting the injection ram speed, which was close to constant at 10 mm/s for ABS and 12 mm/s for HVPC. The acceleration distance was 1.54 mm for ABS and 1.50 mm for HVPC, resulting in an acceleration time of approximately 0.15 s for both polymers. The filling was followed by 4 s of packing phase, with a holding pressure of 40 MPa for the ABS and of 50 MPa for the HVPC (stepped down to 35 MPa). The cooling time was set at 15 s for both polymers. The melt temperature of the ABS was set to 237 °C with cooling water at 17 °C, whereas the melt temperature of HVPC was set to 295 and 95 °C cooling water. The cooling channel is located in the opposite side of the mold half with the glass, together with the ejector system. The same setup was also used in the injection molding simulations.

4.3.2 Results

The temperatures of interest reached steady state after 4 cycles, see Fig. 17. The last cycle is also compared with the last cycle from the axisymmetric and the 3D induction heating simulations. The signal at the sensor T3 is somewhat lower, but the overall temperature distribution seems to agree very well with the 3D induction heating simulation, comparing Fig. 19 to Fig. 13 for ABS and Fig. 21 to Fig. 14 for HVPC.

The simulations were also conducted without the induction heating coil turned on, and the steam temperature was set to 45 and 95 °C for ABS and HVPC, respectively.

The temperature distribution at beginning of filling, end of filling, and end of cooling can all been seen for final cycle in Figs. 18 and 19 for ABS without and with heating turned on respectively. The same for HVPC in Figs. 20 and 21 without and with heating turned on respectively. Looking at the cross section without induction heating, i.e., the glass, heat is slowing build up, since it does not diffuse away as rapidly as in the mold metal material.

The temperature distribution is important for the flow solver, as this essentially is what the polymer "sees" as it flows into the cavity. Looking in Fig. 19 at the beginning of filling and comparing with Fig. 13 from Ansys, the temperature distributions in the cavity surface appear to be in good agreement, and it is indeed somewhat higher in the induction heating simulations. Convergence problems for the transient thermal simulations prevented the use of higher temperature for the steam. Nevertheless, the temperature is above the no flow temperature, and as such the melt is affected by the temperature increase.

One of the challenges is to achieve uniformity of the temperature distribution in the cavity surface. This is difficult to obtain when the coil is not perfectly following the part geometry, and it is also affected by the fact that the heated insert needs to be thick enough to be mechanically stable during filling and packing, i.e., the heat will spread out in the directions away from the cavity surface (Figs. 22 and 23).

The pressure curves from the two pressure sensors and the machine pressure can be seen in Figs. 24 and 28. The experimental and simulated pressures seem to agree in tendency, even though there are some small differences, in both timings and levels. For both materials, there seem to be a slight decrease in pressure for the induction heating moldings. The effect is not larger due to the relatively small section of thin material that the flow needs to fill, and that there is not a pressure sensor positioned in the end of the flow at the T3 location (Fig. 25).

In order to time the filling of the cavity, the following timings of the flow front at different points are defined, see Fig. 26:

• Point A is positioned in correspondence to the first corner in the runner, and the time is defined as the moment at which the melt completely fills up the corner.

• Point B is defined when the melt is at the gate, i.e., when the flow front is just about to enter the cavity.

• Point C indicates when the melt has entered the cavity and the two first corners are filled.

• Point D indicates when the two melt fronts start to develop a weld line, that is they are meeting after the0.5-mm-thick section.

• Point E is defined as when the melt has flown over the location of the last thermal sensors T3.

The results are shown for ABS in Fig. 27 and for HVPC in Fig. 28. Looking at the timings between the experiments with and without induction heating, it is clear that up to the thin middle section, that is, A, B, and C, there is not a large improvement, since the heat is not conducting to the runner region, and even if it was it is thick enough to not freeze through the thickness. Timings at and between D and E do show that the cavity is more easily filled since the timings are lower, especially for the HVPC which in general is more difficult to fill as compared to ABS. For ABS, we see improvements of 30 ms between sections, and for HVPC up 200 ms (also due to the fact that the last region of the cavity is filled during packing without induction heating).

The simulations of the flow timings agree very well for the ABS case, both without and with induction heating. The first verification of the timings without induction heating showed that both ram acceleration and using machine geometry as hot runner to get the effect of all the compressible material were needed to obtain such accurate results, as demonstrated in [41, 42]. This was transferred to the flow simulation together with transient thermal results of the induction heating, and these showed the same trends as in the experiments. They do lag somewhat behind, but the pattern is the same as without heating.

The HVPC does have a larger deviation from the experiment without induction, but in fact the induction heated simulation is really close to the experimental results, which does show a strong thermal dependency

of this material. The material data for HVPC might need corrections at lower temperature or simply the no flow temperature is too high in the simulation.

The visual filling sequence from the high speed camera and from the simulation at the same position without induction heating is shown for ABS and HVPC in Tables 3 and 5, respectively. They show a really good agreement, and the long dragged 'V' shape over the middle section is captured by the simulation, in a similar fashion for each material. In Tables 4 and 6, the induction heating is turned on, and there is a clear indication of that the material does not freeze as without induction. This is true for both materials. Due to the geometrical layout, the flow will always tend to be faster in thicker ribs, since it requires less pressure. So a small air trap will be present in the end of the flow in the top of the middle section. But since a frozen layer is not created with induction, the pressure required for filling over the section does drop, and the flow is able to cross it without hesitation. Also, no clear weld lines/marks are created on the parts with induction heating, showing an improved visual appearance, and mechanical strength (especially for the filled ABS parts without induction heating where the filled 'V' could be pressed out by hand force).

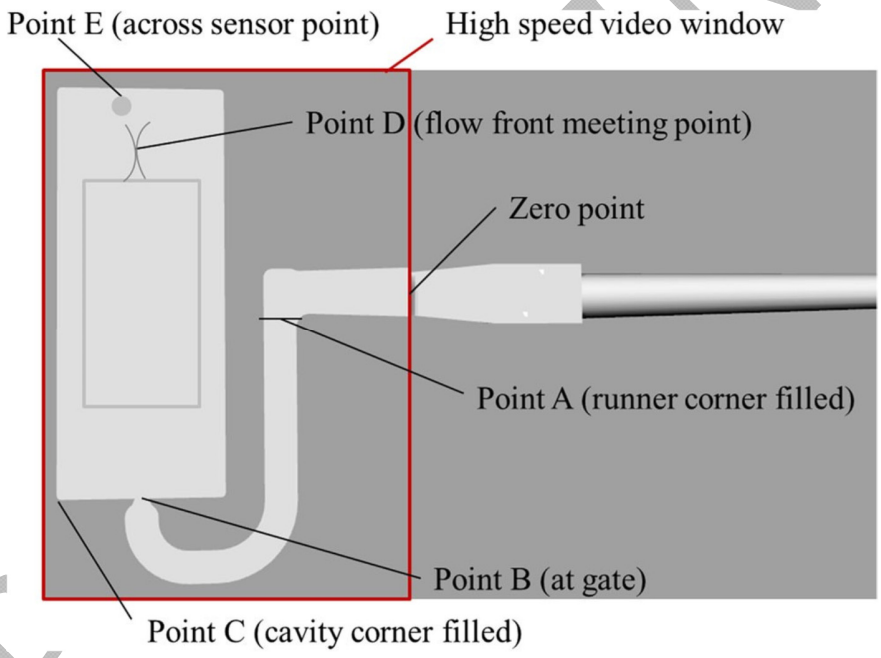

Fig. 26 Points that indicate the timing measurements

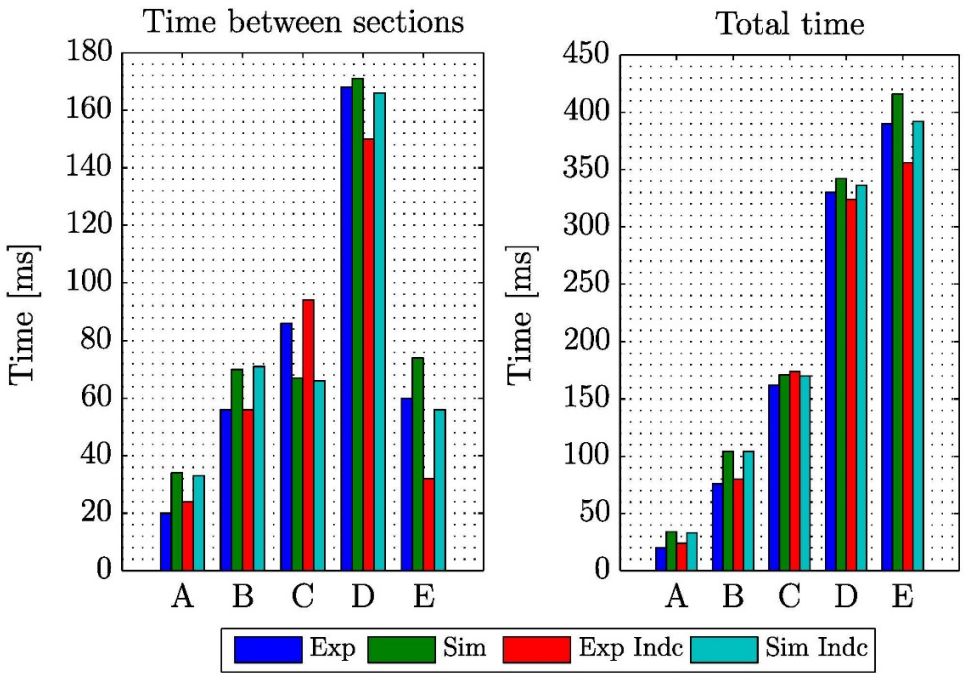

Fig. 27 Experimental and simulated timings compared for ABS

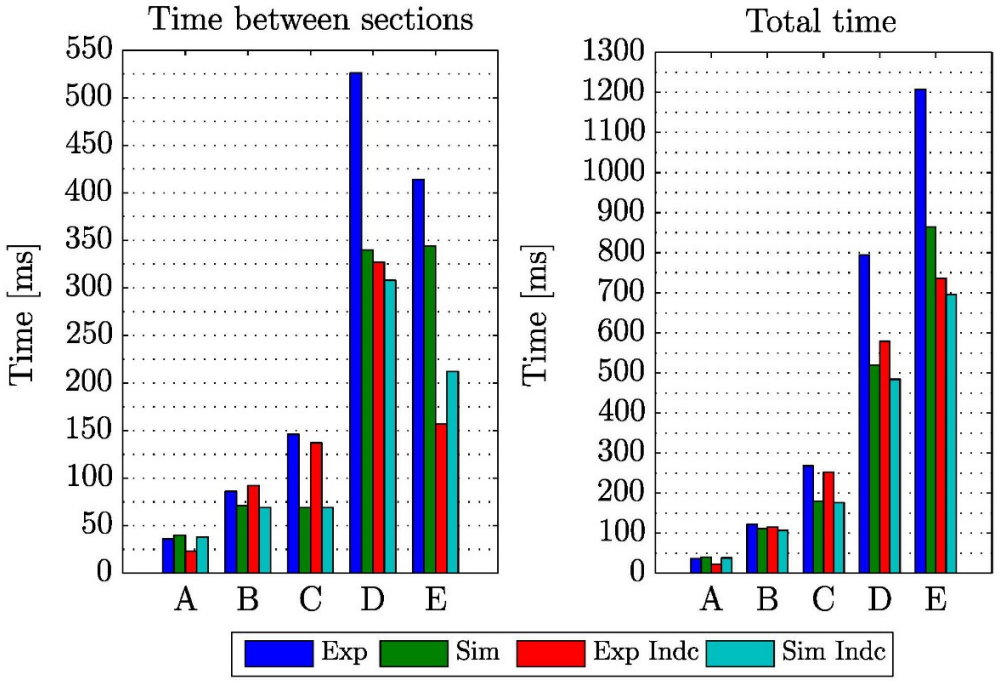

Fig. 28 Experimental and simulated timings compared for HVPC

Table 3 Experiments and simulation results of flow front position, pattern shape, and filling time with ABS without induction heating. Note: The time zero point is set when the flow enters the field of view of the high speed camera

Experiment	Simulation	Experiment	Simulation
			
A: 20 ms	34 ms	D: 330 ms	342 ms
			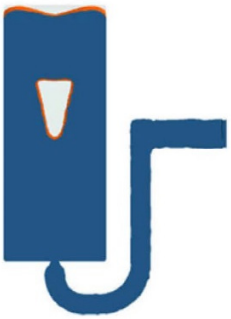
B: 76 ms	104 ms	E: 390 ms	416 ms
			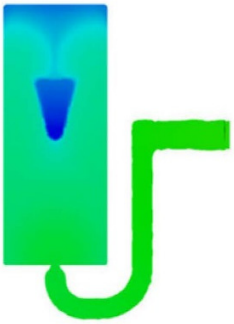
C: 162 ms	171 ms	EoF: 536 ms	593 ms

Table 4 Experiments and simulation results of flow front position, pattern shape, and filling time with ABS with induction heating. Note: The time zero point is set when the flow enters the field of view of the high speed camera

Experiment	Simulation	Experiment	Simulation
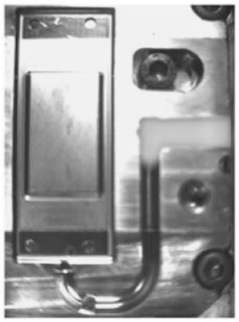			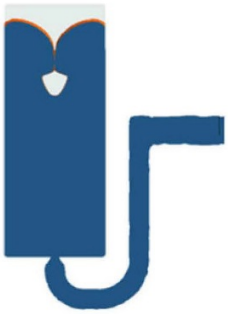
A: 24 ms	33 ms	D: 324 ms	336 ms
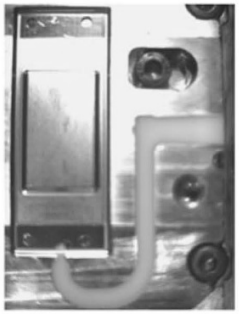			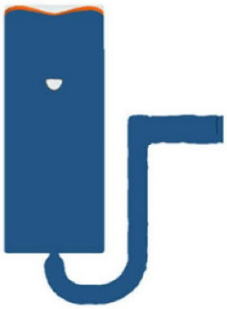
B: 80 ms	104 ms	E: 356 ms	392 ms
			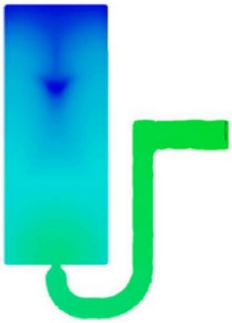
C: 174 ms	170 ms	EoF: 406 ms	424 ms

Table 5 Experiments and simulation results of flow front position, pattern shape, and filling time with HVPC without induction heating. Note: The time zero point is set when the flow enters the field of view of the high speed camera

Experiment	Simulation	Experiment	Simulation
			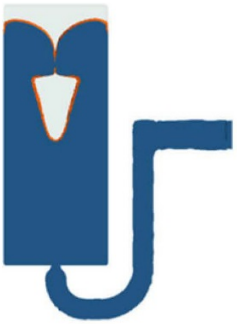
A: 36 ms	40 ms	D: 794 ms	520 ms
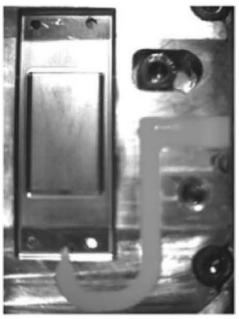		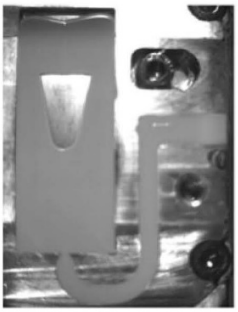	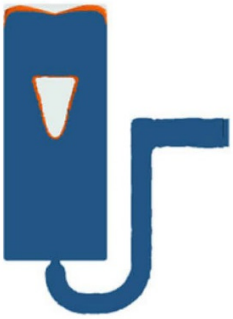
B: 122 ms	111 ms	E: 1208 ms	864 ms
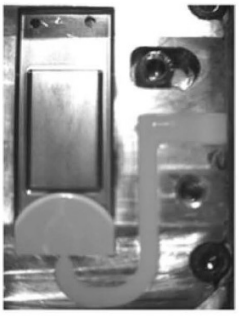		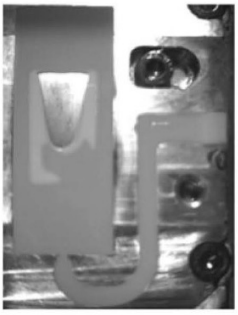	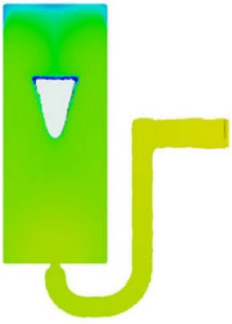
C: 268 ms	180 ms	EoF: 1672 ms	1148 ms

Table 6 Experiments and simulation results of flow front position, pattern shape, and filling time with HVPC with induction heating. Note: The time zero point is set when the flow enters the field of view of the high speed camera

Experiment	Simulation	Experiment	Simulation
		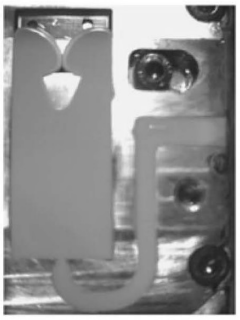	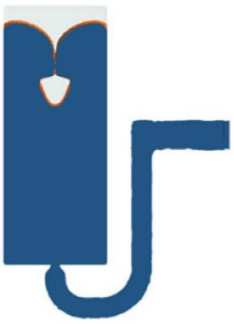
A: 23 ms	38 ms	D: 579 ms	484 ms
		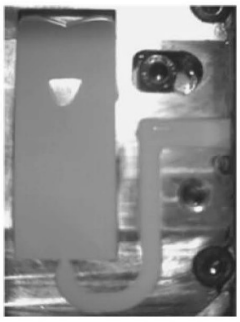	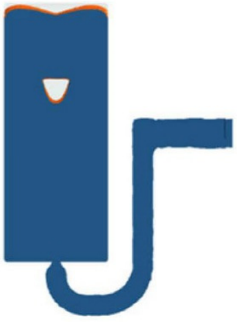
B: 115 ms	107 ms	E: 736 ms	696 ms
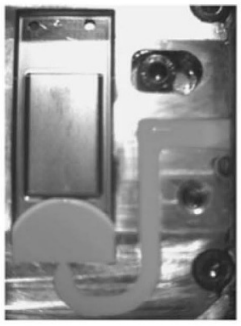		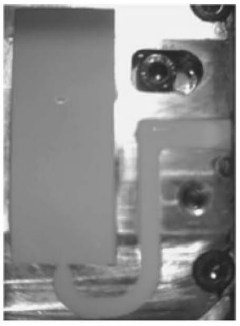	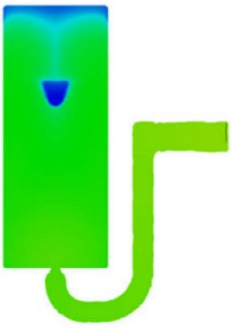
C: 252 ms	176 ms	EoF: 941 ms	956 ms

5 Conclusion

• An approach to simulate integrated induction heating in the tool for the filling of an injection mold has been put forward in the present work

- An axisymmetric nonlinear finite element simulation for the induction heating was used to find the effective linear permeability for the linear 3D analysis;
- 3D simulations of the transient thermal field due to the electromagnetic induction heating were reproduced in the flow solver.

• Experiments using a glass mold with induction heating on an injection molding machine were carried out. The mold was equipped with both thermocouples and pressure sensors, and a high speed camera recorded the flow during filling of the cavity. Two polymer materials ABS and HVPC were tested in the setup.

- Improvements were seen on the filling pattern on the thin section of the part using induction heating. The polymer was able to flow across the thin section without creating a frozen layer large enough to prevent it from flowing, as was observed for the molding without induction heating.

• Simulations of the flow were carried out using real machine speed profiles, including ram acceleration, and machine geometry to include the effect of a large volume in front of the inlet being compressible.

- This led to timings in the flow for the simulations which are comparable to the experimental results from the high speed camera.

• The simulations without induction heating were adapted with a transient thermal analysis with the reproduced thermal field from the 3D electromagnetic‐thermal simulation.

- The results showed the same effect as with the experimental results of the high speed videos of the induction heating moldings. The poor filling behavior across the thin section was remedied using the induction heating.

• A rapid thermal cycle was proved to be feasible with an in-mold integrated coil. Furthermore, it was shown that the process can be modeled with good accuracy. This method can be applied to optimize the design of tools with integrated induction heating coils.

Acknowledgment

This work was carried out as part of the Innomold Project (Innovative Plastic Products and More Energy Efficient Injection Molding Processes) supported by the Danish Council for Technology and Innovation.

A big thanks to IPU for their help with developing the induction heating system, specifically thanks to Christian Ravn (IPU) and Dr. Peter Torben Tang (IPU).

References

1. Yao D, Chen S-C, Kim BH (2008) Rapid thermal cycling of injection molds: an overview on technical approaches and applications. Adv Polym Technol 27:233–255
2. Chen S, Peng HS, Chang JA, Jong WR (2004) Simulations and verifications of induction heating on a mold plate. Int Commun Heat Mass Transfer 7:971–980
3. Chen SC, Peng HS, Chang JA, Jong WR (2005) Rapid mold surface heating/cooling using electromagnetic induction technology
4. Chen S-C, Jong W-R, Chang Y-J, Chang J-A, Cin J-C (2006) Rapid mold temperature variation for assisting the micro injection of high aspect ratio micro-feature parts using induction heating technology. J Micromech Microeng 16:1783–1791
5. Chen SC, Jong WR, Chang JA (2006) Dynamic mold surface temperature control using induction heating and its effects on the surface appearance of weld line. J Appl Polym Sci 101:1174–1180
6. Chen SC, Jong WR, Chang JA, Chang YJ (2006) Dynamic mold surface temperature control using induction and heater heating combnied with coolint cooling. Int Polym Process XXI:457–463
7. Chen SC, Tarng SH, Chiou YC, Tsai TP, Yang WH (2008) Numerical simulation and experimental study on the temperature behavior of pulsed cooling. In: Proceedings of the Polymer Processing Society PPS-24
8. Kwon O-K, Jeong H-T, Yun J-H, Park K (2007) A study on rapid mold heating system using high-frequency induction heating. Trans Korean Soc Mech Eng A 31:594–600
9. Park K, Choi S, Lee SJ, Kim YS (2008) Injection molding for a ultra thin-wall part using induction heating. Trans Korean Soc Mech Eng A 32:481–487
10. Eom H, Park K (2009) Fully-coupled numerical analysis of high-frequency induction heating for thin-wall injection molding. Polym-Plast Technol Eng 48:1070–1077
11. Park K, Kim Y-S (2009) Effects of mold temperature on mechanical properties of an injectionmolded part with microfeatures. J Polym Eng 29:135–153
12. Eom HJ, Park K (2010) Integrated numerical analysis of induction-heating-aided injection molding under interactive temperature boundary conditions. Trans Korean Soc Mech Eng A 34:575–582
13. Park K, Lee S-I (2010) Localized mold heating with the aid of selective induction for injection molding of high aspect ratio micro-features. J Micromech Microeng 20:11
14. Park K, Sohn D-H, Cho K-H (2010) Eliminating weldlines of an injection-molded part with the aid of high-frequency induction heating. J Mech Sci Technol 24:149–152
15. Eom H, Park K (2011) Integrated numerical analysis to evaluate replication characteristics of micro channels in a locally heated mold by selective induction. Int J Precis Eng Manuf 12:53–60
16. Park K, Seo YS, Sohn DH (2011) Automated mold heating system using high frequency induction with feed back temperature control. Int Polym Process XXVI:490–497
17. Huang M-S, Tai N-S (2009) Experimental rapid surface heating by induction for micro-injection molding of light-guided plates. J Appl Polym Sci 113:1345–1354
18. Huang M-S, Huang Y-L (2010) Effect of multi-layered induction coils on efficiency and uniformity of surface heating. Int J Heat Mass Transf 53:2414–2423

19. Huang M-S, Yu J-C, Lin Y-Z (2010) Effect of rapid mold surface inducting heating on the replication ability of microinjection molding light-guided plates with v-grooved microfeatures. J Appl Polym Sci 118:3058–3065
20. Yu J-C, Huang M-S, Liang Z-F, Gu H-H (2011) Intelligent optimization of the replication of injection molding light guide plates using rapid mold surface inducting heating. In: Fourth International Conference on Intelligent Networks and Intelligent Systems
21. Nian S-C, Huang M-S, Tsai T-H (2014) Enhancement of induction heating efficiency on injection mold surface using a novel magnetic shielding method. Int Commun Heat Mass Transfer 50:52– 60
22. Sung Y-T, Lin Y-N, Hwang S-J, Lee H-H, Huang D-Y (2011) Design of induction heating module for uniform cavity surface heating. In: Annual Technical Conference ANTEC, Conference Proceedings
23. Huang CT, Hsien IS, Tsai CH, Chiou YC, Tang CC (2011) The effects of various variotherm processes and their mechanisms on injection molding. Int Polym Process XXVI:265–274
24. Huang CT, Hsieh IS, Tsai CH (2010) The effects of various variotherm processes and their mechanisms on injection molding. In: Proceedings of the Polymer Processing Society PPS-26
25. Kim S, Shiau C-S, Kim BH (2007) Injection molding nanoscale features with the aid of induction heating. Polym-Plast Technol Eng 46:1031–1037
26. Xu RX, Sachs E (2009) Rapid thermal cycling with low thermal inertia tools. Polym Eng Sci 49:305–316
27. Xie L, Ziegmann G (2008) A visual mold with variotherm system for weld line studying micro injection molding. Microsyst Technol 14:809–814
28. Yu MC, Young WB, Hsu PM (2007) Micro-injection molding with the infrared assisted mold heating system. Mater Sci Eng:288– 295
29. Michaelia W, Klaibera F, Scholzb S (2008) Investigations in variothermal injection moulding of microstructures and microstructured surfaces. Multi-Material Micro Manufacture
30. Yang C, Yin XH, Cheng GM (2013) Microinjection molding of microsystem components: new aspects in improving performance. J Micromech Microeng 23:21
31. Shayfull Z, Sharif S, Zain AM, Ghazali MF, Saad RM (2014) Potential of conformal cooling channels in rapid heat cycle molding: a review. Adv Polym Technol 33:24
32. Guerrier P, Hattel JH (2013) Numerical modeling of magnetic induction and heating in injection molding tools. Proceedings NEWTECH 2013 2:35–45
33. Menotti S, Hansen H, Bissacco G, Guerrier P, Tang P (2015) Comparison of two setups for induction heating in injection molding. Int J Adv Manuf Technol
34. Chen S-C, Jong W-R, Chang J-A (2006) Dynamic mold surface temperature control using induction heating and its effects on the surface appearance of weld line. J Appl Polym Sci 101:1174–1180
35. Guerrier P, Nielsen KK, Hattel JH (2015) Temperature dependence and magnetic properties of injection molding tool materials used in induction heating. IEEE Trans Magn 51(9)
36. Guerrier P, Nielsen KK, Menotti S, Hattel JH (Submitted) An axisymmetrical non-linear finite element model for induction heating in injection molding tools
37. Rudnec V, Loveless D, Cook R, Black M (2003) Handbook of induction heating. Marcel Dekker Inc.
38. Ratnajeevan S, Hoole H (eds) (1995) Finite elements, electromagnetics and design. Elsevier
39. Davies EJ (1990) Conduction and induction heating. Peter Peregrinus Ltd., London

40. Labridis D, Dokopoulos P (1989) Calculation of eddy current losses in nonlinear ferromagnetic materials. IEEE Trans Magn 25:2665–2669
41. Guerrier P, Tosello G, Hattel JH (2014) Analysis of cavity pressure and warpage of polyoxymethylene thin walled injection molded parts: experiments and simulations. PPS30
42. Vietri U, Sorrentino A, Speranza V, Pantani R (2011) Improving the predictions of injection molding simulation software. Polym Eng Sci:2542